Wideband Synthetic-Aperture Millimeter-Wave Spatial-Channel Reference System With Traceable Uncertainty Framework

PETER VOURAS [1] (Member, IEEE), BENJAMIN JAMROZ [2], ALEC WEISS[2], DYLAN F. WILLIAMS [2],
RODNEY LEONHARDT [2], DAMLA GUVEN[1], ROBERT JONES [2], JOSH KAST[2],
KATE A. REMLEY [2] (Fellow, IEEE), ROBERT D. HORANSKY [2], AND CAMILLO GENTILE [1]

(Invited Paper)

[1]Wireless Networks Division, National Institute of Standards and Technology, Gaithersburg, MD 20899 USA
[2]RF Technology Division, National Institute of Standards and Technology, Boulder, CO 80305 USA

CORRESPONDING AUTHOR: PETER VOURAS (e-mail: synthetic_aperture_twg@ieee.org).

ABSTRACT This paper describes a wideband synthetic-aperture system and the associated Fourier processing for generating high-resolution spatial and temporal estimates of the signal propagation environment in wireless communication channels at millimeter-wave frequencies. We describe how to configure the synthetic aperture system for high angular resolution by sampling the progression of signal phase across a large planar area in space. We also show how to synthesize discrete measurements of the channel frequency response taken sequentially over a wide bandwidth to create power delay profiles (PDPs) in specified angular directions with high delay resolution. We provide a rigorous uncertainty analysis that can be made metrologically traceable to fundamental physical standards. This uncertainty framework can propagate the errors inherent in the measured signals through to the final channel estimates and derived parameters such as root-mean-square delay or angular spread. We illustrate use of the system in conjunction with two different analysis tools to extract both narrowband and wideband parameter estimates from the synthetic aperture, allowing its use as a stand-alone channel sounder or as a tool for verifying the performance of wireless devices.

INDEX TERMS Channel measurement, measurement uncertainty, millimeter-wave wireless device, over-the-air calibration, wireless system.

I. INTRODUCTION

In much of the world, fifth (5G) and sixth generation (6G) wireless networks are arguably converging towards millimeter-wave frequency bands to support higher data transfer rates. The mid to high-frequency bands from 28 to 100 GHz enable the use of multi-GHz signal bandwidths with existing modulation schemes such as orthogonal frequency division multiplexing (OFDM). The potential commercial applications of these networks is immense and includes industrial internet-of-things (IIoT) in factory settings, wireless connections between computers in data centers, remote medical diagnostics, virtual reality, autonomous vehicles, and many more.

The performance of wireless hardware must often be verified in over-the-air (OTA) conditions, both because some certification bodies require this, and because there typically are no accessible conducted ports. Since the usual deployment environment of a millimeter-wave wireless network will include dense scattering sources, the signal detected at the receiver will contain multipath echoes that can cause inter-symbol interference (ISI). Each multipath component corresponds to a non-line-of-sight propagation path between the transmit and receive antennas and can degrade error-rate performance. In OFDM protocols, a guard interval is inserted between symbols to mitigate the detrimental effects of delay spread caused by multipath. However, for the wireless

systems engineer building a front-end, it is important to not only understand the signal propagation environment but also the limitations of the available hardware. For example, commercial transceivers may suffer from non-ideal beam patterns caused by parasitic effects such as mutual coupling between phased array elements.

This paper describes a wideband millimeter-wave synthetic aperture system designed, tested and validated by the National Institute of Standards and Technology (NIST) for use as a high-performance wireless measurement instrument. We detail the performance characteristics, provide a comprehensive measurement uncertainty framework that includes correlations between components of uncertainty and present back-end analysis techniques for wideband and narrowband applications. Such a system may be used for traceably characterizing spatial channels for OTA device testing, for verifying the performance of other channel measurement systems, or for test chamber calibration [1].

The measurement and analysis techniques presented here are significantly different from channel sounding, as the goal is to provide the best possible environment characterization using a combination of (1) rigorous, high-dynamic range, non-real-time measurements; (2) a comprehensive uncertainty analysis that includes correlations between components of uncertainty; and (3) computationally expensive, but highly accurate post-processing analysis methods to characterize the resolution of the system. Taken in combination, the NIST Synthetic Aperture Measurement Uncertainty for Angle of Incidence system, also known as SAMURAI, may be considered to be a metrology grade OTA calibration tool as opposed to a channel sounder, developed with the goal of allowing increased confidence in the assessment of a user's Device Under Test (DUT) under a variety of spatial and temporal channel conditions.

A synthetic aperture (sometimes called a virtual array) in the context of the present work refers to a collection of sequential digitized measurements made using a single receiver channel by precisely moving a receive antenna (also called a probe) to different locations in space so as to capture the electromagnetic fields propagating across the observation plane of the aperture. This measurement technique should not be confused with synthetic-aperture radar which relies on an aircraft and Doppler frequency measurements to create radar images of the environment. The synthetic aperture system we discuss here, along with the associated post-processing and Fourier beamforming algorithms, are capable of resolving closely-spaced scatterers in static wireless communication channels. A primary contribution of this paper is a detailed description of the process involved in designing a synthetic aperture measurement system to meet the specifications of the anticipated use case.

Synthetic apertures have been described in the channel sounding literature with varying levels of rigor and detail. Some of the recent results related to synthetic-aperture measurements include an approach [2] for multiple-in multiple-out (MIMO) radar. An investigation into the impact of

position errors is given in [3], however this work does not leverage an optical camera system as described here. The use of a VNA as a channel sounder is described in [4], [5], but the sounder does not include a synthetic aperture. One-dimensional linear and three-dimensional cubic sampling lattices are the subject of [6], [7], [8], however, these contributions do not address planar synthetic apertures. Unique approaches to synthesize an aperture through platform motion are in [7], [9], [10], [11], [12], but these approaches are often difficult to implement in practice. Typically, synthetic-aperture systems based on VNAs are short range due to the available length of cables, but [13] describes a long-range VNA-based sounder for outdoor measurements.

Sampling lattices that exhibit rotational symmetry, such as circular or cylindrical, are desirable because they offer an omnidirectional view of the environment. An approach for creating circular synthetic apertures is given in [14]. Cylindrical and circular synthetic apertures will often require more spatial samples to implement than the planar aperture described here. Note that the geometry of the aperture will determine the basis functions used to beamform the received data. For example, a planar array utilizes steering vectors that describe a linear phase progression across the aperture. The far field pattern of a circular aperture will be described in terms of Bessel functions. Planar apertures are almost always used for phased array antennas in commercial wireless devices and are therefore the focus of this paper.

This paper is the first to describe the use of synthetic apertures with uncertainties as a metrology standard to calibrate other wireless hardware using over-the-air signals. The NIST SAMURAI synthetic-aperture system serves as a calibrated testbed for mmWave device assessment by extending "comparison-to-reference" methods in which the measurement system itself becomes the reference rather than a physical artifact [1]. In this new approach to calibration for OTA test and measurement scenarios, we may traceably characterize complicated, non-ideal channels with a higher degree of spatial and temporal resolution than the DUT or system to be tested. The performance of a DUT placed into this well-characterized environment may then be assessed under these known conditions.

Our initial work in this area illustrated the use of a synthetic-aperture system to estimate the electromagnetic fields inside a loaded reverberation chamber at microwave frequencies [15]. SAMURAI, focusing on millimeter-wave frequencies, can serve as a reference system for OTA calibrations of metrics derived from the spatial and temporal characteristics of wireless devices with integrated active antenna systems. By incorporating a large-signal network analyzer, SAMURAI can also be used to characterize environments into which systems that incorporate integrated downconverting antenna arrays will be placed, while maintaining cross-frequency phase calibrations [16].

The remainder of the paper is organized as follows. Section II provides the approach and methodology for an OTA calibration of an RF front-end with an integrated antenna.

Section III describes the beamforming process, some of the measurement attributes of SAMURAI and provides a methodology for setting system parameters. Section IV provides an overview of the SAMURAI hardware design. Section V outlines the uncertainty and error analysis for SAMURAI measurements. Section VI provides an example of SAMURAI's use as a reference instrument with both narrowband and wideband parameter-estimation algorithms. These results consist of measurements taken in a controlled lab setting during experiments designed to demonstrate the resolution capabilities of SAMURAI. The empirical results illustrate SAMURAI's capabilities as an OTA reference system that can be used to verify the outputs of other wireless hardware devices in addition to SAMURAI's use as a stand-alone channel sounder.

II. A TRACEABLE APPROACH FOR CALIBRATING OVER-THE-AIR MEASUREMENTS

Two primary methods exist for calibrating measurement hardware. The first approach relies on using standards which are physical realizations of a measurement unit. If a standard of the desired measurement unit (e.g. 1 V) is provided at the input to a device, then the measured result can be compared to the value of the standard. This calibration approach is the most accurate but standards may not be available for every quantity to be measured.

A different approach to calibration is to compare the measurement result from a DUT to the output of another instrument that has been calibrated via a traceable path back to the relevant standards. In this procedure, the uncertainty of the reference instrument must be lower than the DUT. For some devices with integrated components such as antennas within RF front ends, a comparison-to-reference approach such as this is the only viable calibration method. Because of the rigorous uncertainty framework used to develop the SAMURAI system, it is ideally suited for providing the necessary reference measurement scenarios where devices are calibrated by comparison.

Often OTA calibration is necessary because the RF analog output appearing at the output of the DUT's front end will differ from the actual signal that was incident on the receive antenna due to the non-ideal response of the DUT, potentially including distortion in both the temporal and, for beam-forming antennas, spatial domains. Comparing the analog output of the device's front end to the expected output derived from the fields measured by a reference receiver whose spatial and temporal specifications exceed those of the DUT may be used to understand the non-idealities of the device or to extract calibration coefficients that correct future measurements made with the device.

Due to the wide array of temporal and spatial characteristics of the channel and the way in which these characteristics interact with non-ideal receivers, specific channel conditions will often result in different sets of calibration coefficients. This means that, in order to calibrate the DUT's front end, the reference system must be able to perform measurements with

temporal and spatial characteristics that exceed those of the anticipated use cases for the DUT. The versatility of SAMURAI is especially well-suited for calibrating the spatial and temporal resolution of a device's front end because the angular and delay resolution of a synthetic aperture can be tailored by the user to match the angular and delay resolution of the DUT. Specifically, the dimensions of the sampling lattice determine spatial resolution, with a larger aperture providing a narrower beamwidth and higher angular resolution. Further, the delay resolution can be set by adjusting the measurement bandwidth (to the upper bound of the VNA hardware). As the SAMURAI system can exceed the accuracy and the spatial and delay resolution of most DUTs, the SAMURAI measurements can then be filtered in both the temporal and spatial domains to match the expected performance of the DUT but with greater accuracy of measurement. These aspects will be described in more detail in Section III.

The vast majority, if not all, of commercial wireless devices with phased array antennas implement Fourier processing using an analog beamformer. Therefore, wideband Fourier processing is also proposed in this paper for use as a performance baseline for comparison. An innovation described in this paper is the consideration of joint spatial and temporal resolution performance. Typically, delay resolution and angular resolution are analyzed separately. However, in our proposed approach if two point scatterers cannot be separated in one measurement domain (e.g. spatial or temporal) but can be distinguished in the other domain (e.g. temporal or spatial) then they are still resolvable. We illustrate this approach by constructing a wireless channel from point sources (e.g. aluminum cylinders) deliberately placed in close proximity in the angular or delay domains. Together with the measurement scenario, an algorithm is presented that creates "delay slices" of the channel impulse response that clearly distinguish the closely-spaced cylinders. Delay slices illustrate spatial power density over all angles of arrival (e.g. simultaneously over azimuth and elevation) for a fixed value of time delay. Integrating each delay slice over the angle coordinates yields the total power received at the synthetic aperture versus time delay. Local peaks in this time series represent the arrival times of discrete multipath signals of interest.

Another key aspect of our OTA calibration approach is the development of a complete framework to capture the uncertainties in the SAMURAI system. We first correct for known errors in the measurement system and then incorporate the remaining errors into the uncertainty analysis. Our uncertainty analysis preserves the correlations that may exist between different sources of uncertainty. Such correlations can have a significant effect on the combined uncertainty in a measurement, especially at millimeter-wave frequencies. See, for example, Section V-B of [17]. Examples of such correlation include frequency dependent ripple caused by impedance mismatch, or the use of the same VNA calibration kit (having the same systematic errors in the definitions of the mechanical standards) to characterize various parts of the system. Our extensive uncertainty framework is described in Section V.
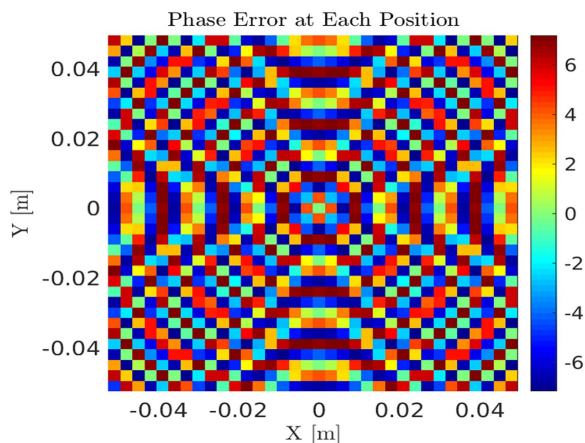
FIGURE 1. Plot illustrates phase error (deg) at each array element. Maximum phase error corresponds to $\lambda/50$ error in *xy*-position of array element. Errors are sinusoidally correlated across the aperture.
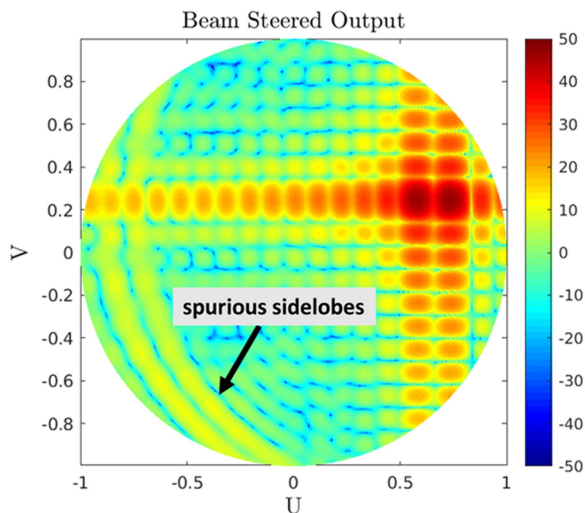

FIGURE 2. Beamformed array output (dB) for two signal sources showing ring of spurious sidelobes caused by correlated phase errors.

An example of the impact of correlated errors in synthetic-aperture measurements is that they can contribute to spurious outputs. For example, Fig. 1 illustrates a progression of correlated phase errors across a planar synthetic aperture. During the beamforming operation, these errors are effectively coherently summed together and produce the rings of spurious sidelobes shown in Fig. 2 as they alternately add in and out of phase. The sidelobe artifacts are easy to misconstrue as energy from the environment and can lead to incorrect results in an OTA calibration.

The approach proposed in this paper for calibrating a DUT front end is to compare the DUT output as measured in a specific channel to a well-characterized reference measurement of the same channel. We create and characterize the channel in a repeatable laboratory environment to assess the performance of the device under the nearly identical channel conditions. Channel nonidealities such as unintentional reflections are included in the reference measurement because the SAMURAI

system captures the entire field of view. Thus, no assumptions need to be made about the test environment.

The calibration procedure will typically consist of steps such as these: 1. Configure the reference system to provide better temporal and spatial resolution than the DUT. This would typically be accomplished by creating an array with the SAMURAI system that exceeds the number of elements in the DUT, exceeds the bandwidth of the DUT and acquires data on the same or smaller frequency increments than the DUT. Methods to obtain these system parameters are discussed in Section III-B and III-C.

2. Measure the environment (channel) in which the DUT will be assessed, either in an enclosed chamber or in an open laboratory environment. Either way, the SAMURAI system is used to characterize the channel in terms of key metrics such as RMS delay spread, RMS angle spread, or others. As mentioned above, unique in our approach is the propagation of uncertainties through to the metrics we calculate. That is, the uncertainties associated with our reference-system hardware are included in the channel characterization.

3. The device under test is then placed into the characterized channel and its performance is measured. Because the SAMU-RAI system has been configured to provide better resolution (spatially and temporally) than the DUT, it is often possible to separate non-ideal channel effects from non-ideal device performance. The resolution of the SAMURAI reference system can also be filtered to match that of the DUT in post processing. This allows a user to see the best performance that could be achieved if the uncertainties associated with their DUT were on the order of the SAMURAI reference system. This approach was described in [16], where the spatial-temporal performance of a 28-GHz downconverting phased array was compared to that of the SAMURAI system. The resolution of the SAMURAI system was filtered to match that of the phased array, allowing the identification of spurious emissions from the array.

Creating and assessing specific, repeatable channels with a reference system represents a new approach to calibrating the angular and delay resolution of a DUT or for testing processing functions such as beam-steering logic. By comparing their output to the reference system's output under well-characterized channel conditions, users can observe both systematic errors (which may be observed as a bias or offset between the two outputs) and random errors (which may be observed as a spread about the mean) in commercial hardware devices and algorithms.

III. BEAMFORMING AND MEASUREMENT ATTRIBUTES OF THE SYNTHETIC-APERTURE REFERENCE SYSTEM

There are many possible implementations of direction finding in synthetic-aperture systems. One approach which also yields reliable estimates of signal source power is delay-and-sum beamforming. This approach however may not resolve objects that are closely spaced in angle within a single beamwidth as illustrated in Fig. 3. An advantage of synthetic apertures is that the array size can be made large so as to reduce the angular
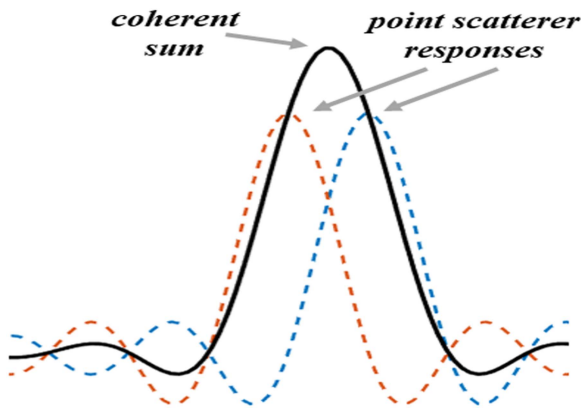
FIGURE 3. Plot showing coherent summation of two sinc functions in close proximity.

width of the mainbeam and thereby provide greater angular resolution.

The processing described in this paper provides a robust and accurate implementation of wideband beamforming. The Fourier processing steps are validated using results from experiments that determine the resolution capabilities of the synthetic aperture. The output of the Fourier processing steps can be specified in either spherical, azimuth-elevation, or sine-space coordinates. The wideband beamforming algorithm defines complex array-element beam-steering weights that align the phases of the signals arriving at the aperture from a single direction. After coherently summing the complex-weighted array-element signals, a directional beam in space is formed that provides a reliable estimate of the signal power received from the beam's pointing angle. The results described in this paper are for an $M \times N$ rectangular grid of uniformly spaced spatial samples.

A. ARRAY COORDINATE SYSTEMS

The rectangular synthetic aperture (also called a planar array) considered in this paper specifies spatial samples on a uniform grid in the xy-plane with the z-axis along the boresight direction normal to the xy-plane. The spherical angle θ in the interval $[0, \pi]$, or $[0, \pi/2]$ in the forward hemisphere only, is measured between the z-axis and the beam-pointing direction. The spherical angle ϕ in the interval $[0, 2\pi]$ is measured in a counter-clockwise direction between the x-axis and the plane of beam scan. The projection of beam-steering directions from the forward-looking unit hemisphere down onto the xy-plane yields the u and v-direction cosines which can be used to specify beam-steering directions in a sine-space coordinate system [18], [19].

The sine-space coordinate system has desirable properties for specifying the array response (beam pattern) and beam-steering directions. First, the array response is equivalent to a spatial Fourier Transform when written in sine space coordinates. Second, the array response is invariant with respect to scan angle (the pointing direction of the main beam) when plotted in sine space. In other words, as the beam is steered,

every point in the array response is translated by the same amount and in the same direction as the main beam peak and the shape of the beam pattern does not change. Angle transformations between spherical, azimuth/elevation, and sine-space coordinates are listed in [20], [21], [22].

B. ANGULAR RESOLUTION VERSUS FREQUENCY

When describing a synthetic aperture, the term "array element" is sometimes used to refer to each spatial sample in the aperture. The far-field response in spherical coordinates (θ, ϕ) for an array of $M \times N$ identical elements in the xy-plane is given by [18],

$$B(\theta, \phi) = E(\theta, \phi) \sum_{m=0}^{M-1} \sum_{n=0}^{N-1} w_{mn} e^{jk(x_m \sin\theta \cos\phi + y_n \sin\theta \sin\phi)}$$

(1)

where $E(\theta, \phi)$ refers to the array element antenna pattern, the wavenumber $k = 2\pi/\lambda$, λ is the operating wavelength (in meters), and w_{mn} is the array element weighting. The summation term in (1) is called the array factor. Conceptually, the array response is equal to the element pattern multiplied by the array factor. The nominal far-field distance from a radiating array is at least $2D^2/\lambda$, where D is the dimension of the array in the corresponding principal plane [21].

In a planar lattice where d_x and d_y denote the distance between array elements in the x and y directions, the array element coordinates in (1) are $x_m = md_x$ and $y_n = nd_y$. Eqn. (1) is easily recognized as a two-dimensional spatial Fourier transform after substituting the change of variables $u = \sin\theta \cos\phi$ and $v = \sin\theta \sin\phi$ [18],

$$B(u, v) = E(u, v) \sum_{m=0}^{M-1} \sum_{n=0}^{N-1} w_{mn} e^{jk(md_x u + nd_y v)}. \quad (2)$$

A consequence of (1) and (2) is that the directivity of the probe antenna determines the scan angle limits of the beam-formed synthetic aperture output. For example, a high-gain probe antenna will severely attenuate the array factor at high scan angles, thereby limiting the field of view of the synthetic aperture. It is possible to measure and de-embed the antenna pattern from the results, as was done in [23]. An alternative is to use an open-ended waveguide with a broad beam pattern as the probe antenna.

The plots in Figs. 4 and 5 show azimuth cuts of the beam-formed outputs at 26.51 and 40 GHz respectively for the SAMURAI measurements of two aluminum cylinders placed on an optical table in a lab setting. The red lines correspond to the actual location of the cylinders. The spatial sampling lattice was a square 35×35 grid with three mm spacing between samples. The cylinders have a diameter of 2.54 cm (one inch) and are placed close together to stress the angular resolution capability of the synthetic aperture.

The nominal angular resolution is equal to the width of the main beam which is proportional to the linear dimensions of the aperture in each principal plane [18]. The number of wavelengths that fit along each dimension D of the aperture
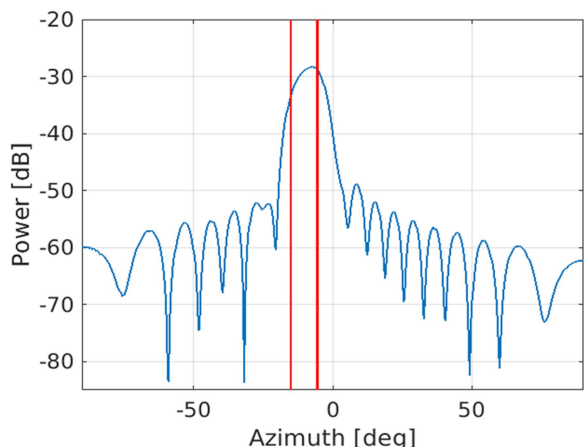
FIGURE 4. Beamsteered array output power, in dB relative to the LSNA's transmitted power, with two closely spaced aluminum cylinders in the channel. At 26.51 GHz, the cylinders cannot be resolved (from [22]).
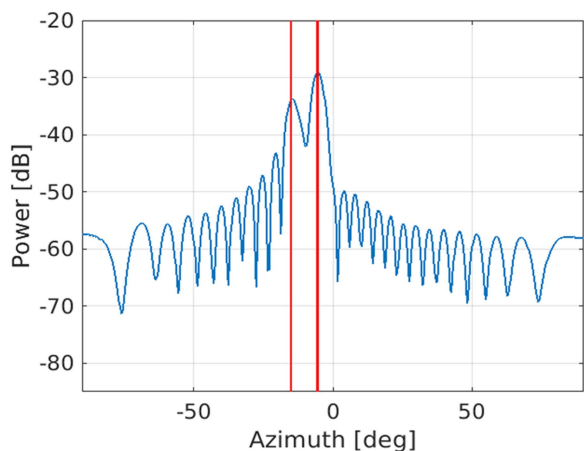

FIGURE 5. Beamsteered array output power, in dB relative to the LSNA's transmitted power, with two closely spaced aluminum cylinders in the channel. At 40 GHz, signal returns from each cylinder can be resolved (from [22]).

determine its electrical length, D/λ. For constant spacing between spatial samples, as the frequency increases, the electrical length of the aperture gets larger and therefore the beamwidth decreases. Consequently, the two cylinders that are not resolvable at 26.51 GHz can be well separated at 40 GHz.

A useful way to quantify the width of the main beam and the angle resolution of the aperture is to compute the two-sided, three-dB beamwidth as the fraction of the array response that exceeds the peak value minus three dB. Using this approach, the smallest SAMURAI beamwidth is 2.9° at 40 GHz and the maximum beamwidth is 4.4° at 26.5 GHz. The Rayleigh approximation (3.3° at 40 GHz) for the azimuth or elevation beamwidths is equal to λ/D radians, or one over the electrical length of the corresponding aperture dimension.

C. OTHER SYSTEM PARAMETERS

As previously mentioned, the SAMURAI synthetic aperture system uses a VNA as the signal transmitter and receiver. In this configuration, the transmit antenna is connected through a coaxial cable to port 1 of the VNA and the receive probe located some distance away is connected to port 2. The VNA signal source launches a sinusoidal tone towards port 1. Some of the incident energy will reflect off port 1 and travel back to the signal source, although most of the energy will radiate through the transmit antenna and propagate into the environment. Some of this energy will arrive at the receive antenna, where it is either absorbed in a load (the receive probe antenna), or is reflected back into the environment. The transmission parameter, S_{21}, is used in the computations described in this paper to represent the complex transfer function between the transmit and receive antennas at the radiated frequency.

In the SAMURAI configuration used in this paper, the VNA measures S_{21} in $\Delta f = 10$ MHz increments between 26.5 and 40 GHz. The bandwidth B of 13.5GHz determines the delay resolution $\Delta\tau$ as in [24],

$$\Delta\tau = \frac{1}{B} = 0.074 \text{ nsec(or 2.2 cm).} \tag{3}$$

Theoretically, the inverse Fourier transform $y(t)$ of the frequency domain channel measurements over all frequencies may be time aliased. However, in the event that the channel impulse response $h(t)$ is time limited to a duration no greater than $1/\Delta f$, then the shifted replicas $h(t - 2\pi n/\Delta\omega)$ do not overlap and $y(t)$ is not time aliased. Thus, the maximum unambiguous delay T that can be measured using frequency domain sampling is equal to one over the frequency step size, or $T = 1/\Delta f = 1/10$ MHz $= 100$ nsec (29.96 meters).

In the case of SAMURAI, the channel frequency response is sampled over a band-limited range, and not over all frequencies. The default frequency step size of 10 MHz provides 1351 samples over the 13.5 GHz measurement bandwidth. After an inverse Fourier Transform, there will be 1351 delay samples between 0 and $T = 100$ nsec which effectively results in a sample rate of $f_{sam} = 13.5$ GHz, which is less than the highest frequency component at 40 GHz. Thus, it seems that the power delay profiles (PDPs) computed using SAMURAI may still be time aliased. For band-limited signals, however, sampling at a rate f_{sam} lower than Nyquist does not create aliasing if,

$$f_{sam} \geq qB \text{ where } 1 \leq q \leq \left\lfloor \frac{f_{max}}{B} \right\rfloor. \tag{4}$$

Sampling the PDPs at a temporal rate equal to the measurement bandwidth, or $f_{sam} = B = 13.5$ GHz, satisfies the bandpass sampling constraints given in (4) since the ratio $40/13.5 = 2.96 \approx 3$ is nearly an integer. Thus, any temporal aliasing in the measured PDPs will be negligible.

With VNA receivers, the dynamic range of a single measurement will depend on the intermediate frequency (IF)

TABLE 1 SAMURAI System Configuration: 2-Cylinder Experiment

Synthetic Aperture Sub-System Parameters
1. Transmit and receive antennas Type: WR-28, 17 dBi waveguide horn E/H plane one-sided 3-dB beamwidth: 23°/24° Bandwidth: 26.5 - 40 GHz Polarization: Linear
2. Antenna positioner Robotic arm: Mecademic Meca500* Number of positions: 1225
3. Synthetic-aperture sampling lattice Planar grid: 12.6 cm width and 12.6 cm height Sample spacing: 3.7 mm ($\lambda/2$ at 40 GHz)
4. Vector network analyzer Frequency range: 26.5 GHz - 40 GHz Measurement bandwidth: 13.5 GHz Frequency step size: 10 MHz resulting in 1351 frequencies IF bandwidth: 100 Hz Reference planes: Coaxial connector at coaxial-to-waveguide adapter Dwell time: 1 ms *Mention of product names does not imply endorsement by NIST. Other products may work as well or better.*

FIGURE 6. System block diagram including the receive (Rx) antenna mounted on the scanning robotic arm; the fixed horn transmit (Tx) antenna; and a multiple-camera system for tracking the position of the Rx antenna and objects in the channel. A custom Python code controls the robot and the LSNA. [30].

bandwidth setting and the amount of sweep-to-sweep averaging performed. The SAMURAI configuration described here uses a 100 Hz IF bandwidth and no averaging applied to the data. The resulting dynamic range calculated over the measurement bandwidth is close to 90 dB [25]. The maximum specified VNA dynamic range of 120 dB corresponds to a 10 Hz IF bandwidth with no averaging.

IV. SAMURAI HARDWARE DESCRIPTION

SAMURAI, the NIST synthetic-aperture system, is based on a large-signal network-analyzer (LSNA) and is capable of a variety of measurements; from characterizations of three-dimensional multipath channels to OTA device and hardware verification in controlled laboratory environments. SAMURAI was designed to provide traceable measurements and to evaluate the inherent measurement uncertainties as discussed in Section VI. The system is reconfigurable, allowing it to be applied to a variety of wideband and narrowband mmWave measurement scenarios, including the characterization of up-converting and down-converting phased arrays [16]. Measurement parameters for a configuration used in this paper are given in Table 1.

LSNAs are very similar to conventional VNAs in that they determine the complex scattering parameters of a network by computing the ratios of forward and backward waves arriving at the measurement ports. LSNAs can also measure the amplitudes and cross-frequency phases of the waves by use of power and phase calibration standards. These calibrations can be made traceable to fundamental physical quantities after propagating the measurement uncertainties to the final result. As a national metrology institute, NIST's goal with the SAMURAI system is to provide traceable wireless channel
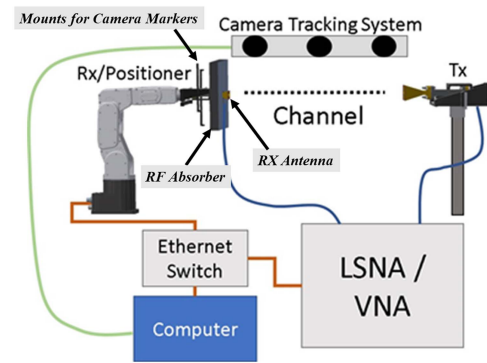
measurements using the framework and procedures described in this paper.

The LSNA provides a wideband measurement capability with a high dynamic range. Many other OTA measurement systems also utilize VNAs for the same reason [26], [27], [28]. However, using a VNA or LSNA over large bandwidths comes at the expense of speed. For example, synthesizing a 35-by-35 planar aperture with 1225 elements and a 13.5 GHz measurement bandwidth with an IF bandwidth of 100 Hz can take over eight hours to complete. The stability of a measurement over this long time period may be affected by temperature and humidity, the location and vibration of scatterers in the channel, and drift in the measurement system [29]. Uncertainties due to these and other effects in SAMURAI measurements are calculated using a Monte-Carlo analysis within the NIST Microwave Uncertainty Framework (MUF), as described in Section VI.

For the work presented here, the synthetic-aperture system includes a fixed transmit antenna, a precise positioner consisting of a robotic arm that moves the receive antenna, and measurement equipment to transmit and receive RF waveforms as shown in Fig. 6 [30]. The use of this robotic arm provides position accuracy below 100 μm as determined by an optical camera system that estimates the actual positions of the robot. The probe antenna of the SAMURAI system mounted onto the tip of the robotic arm can be moved to points along a specified spatial sampling lattice with a repeatability of 5 μm [31]. The robotic arm has a rated payload capacity of 500 grams and it moves via six joints that can be independently controlled using the built-in software interface or with external software, such as Python [32]. The tip of the robotic arm can reach points inside an arc of radius equal to 260 millimeters when only rotating the last three joints of the arm and keeping the first three joints fixed.

The probe antenna used in the 2-cylinder experiment is a pyramidal horn attached to rectangular waveguide (see Table 1). An open-ended waveguide (OEWG) antenna will
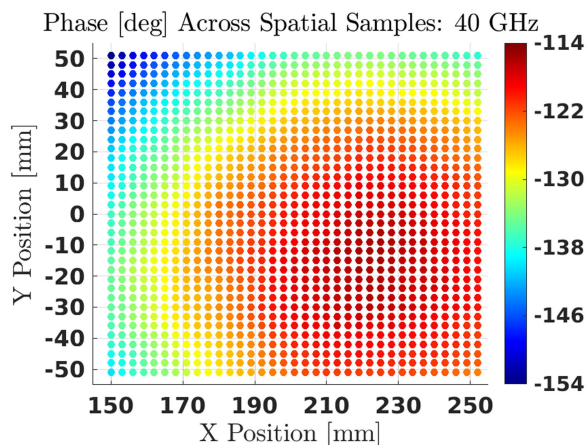
FIGURE 7. Measured phase, in degrees, across the aperture for a line-of-sight signal at 40 GHz. A difference of approximately 40 degrees can be seen across the aperture.

FIGURE 8. Measured LOS array response at 40 GHz: Elevation vs azimuth.

FIGURE 9. Diagram of experiment of scattering from two closely spaced aluminum cylinders. RF absorber has been placed on the table top to minimize scattering from the environment.

provide a wider beamwidth, which allows for larger scan angles in the beamformed output of the synthetic aperture. While such OEWG probes will provide a wider beamwidth, the measurements described here required the additional gain of the horn antennas and did not require a wide scan angle. With either antenna type, the gain pattern of the antenna and the corresponding uncertainties, are accounted for in the synthetic-aperture analysis, as discussed in Section VI.

To use SAMURAI as a reference system to which other measurements can be compared for over-the-air (OTA) calibration applications, an external camera system is used for position location of the antennas and reflecting objects in the test environment. By mounting at least multiple small infrared reflective markers on the antenna frame (10 were used here), the camera system can provide the locations of spatial samples and the orientation of the antenna as it moves through the sampling lattice. Markers placed on objects in the scene can also be used to validate estimated multipath angles and delays computed in the post-processing steps. The data provided by the camera system supports a rigorous analysis that incorporates into the uncertainties surrounding the final synthetic aperture measurements the positional errors associated with the actual placement of the sampling lattice in space and the orientation of the probe antenna.

Fig. 7 illustrates the phase measured across the spatial samples of a 35-by-35 planar synthetic aperture created in a laboratory setting with a strong LOS signal. Fig. 8 illustrates the beamformed output at 40 GHz in azimuth and elevation coordinates for this LOS signal. Because the array is uniformly weighted (i.e. unity amplitude scaling is applied to each array element), the first sidelobes of the array response are approximately 13.2 dB below the mainbeam peak.

In one stable, controlled configuration often used at NIST, the SAMURAI system is placed on an optical table which minimizes position uncertainties due to vibration and allows for scatterers to be repeatably placed in the channel. A picture
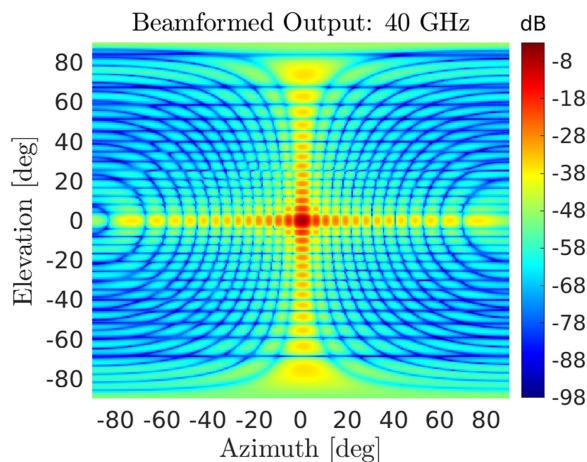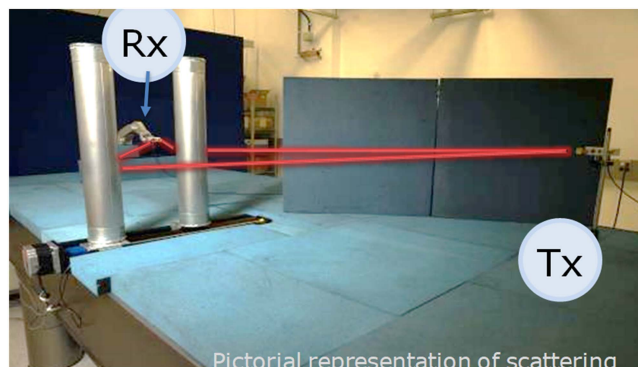
of the SAMURAI system configured with two cylinders on the optical table to create reflections at variable path lengths and angular separations can be seen in Fig. 9. The total length of the optical table equals 4.3 m and its width is 1.5 m. The usable length of the table in front of the robot positioner is approximately 3 m.

V. TRACEABILITY AND UNCERTAINTY ANALYSIS
A. EFFECT OF CORRELATED ERRORS ON UNCERTAINTY ESTIMATION

One of the goals of the NIST SAMURAI project is to provide quantitatively accurate channel responses and an uncertainty estimate with traceability to fundamental quantities. By traceability, we refer to the definition of metrological traceability in [33] as "an unbroken metrological traceability chain to an international measurement standard or a national measurement standard." Our synthetic-aperture system is a multi-faceted system and, therefore, the full uncertainty analysis is complex and spans many disparate factors. As uncertainty analysis and traceability are core aspects of this work, the system has been designed to provide for this. One drawback of a rigorous uncertainty analysis is that it increases

the necessary data acquisition time. For OTA calibration applications, the SAMURAI system serves as a reference, intended for the verification of other systems.

An important aspect of our uncertainty analysis framework is that we propagate errors induced by physical sources, e.g. the mechanical tolerances of VNA calibration standards, through to the final system response. We implement our uncertainty analysis by leveraging Monte Carlo simulations that also preserve the correlations that may exist between different sources of uncertainty. Therefore, our uncertainty framework yields more robust error estimates than the typical root-sum-of-squares method that may neglect correlated behavior between error sources. A desirable outcome of this uncertainty analysis is that it provides accurate estimates for complicated system responses such as power-angle-delay profiles or even communication metrics such as error vector magnitude [34]. However, this analysis can be computationally expensive since it relies on many Monte Carlo samples for statistical significance. In this section, we outline our methodology for maintaining traceability and evaluating the uncertainty in measurements made with our system, including components such as VNA calibrations, cable movement, antenna responses, positioning errors, and reflections off of positioners.

B. LSNA/VNA CALIBRATIONS

The LSNA or VNA is calibrated before every experiment. For the results presented in this paper, a short-open-load-thru (SOLT) WR-28 calibration was performed. Uncertainty in the dimensions of the physical artifacts used to calibrate the LSNA or VNA is propagated through to the final output of our Fourier processing. This can be traceable to fundamental quantities [35]. In other words, every individual S-parameter measurement in our synthetic aperture has an estimate of uncertainty that can be made traceable to a physical unit, such as, the meter, second, and impedance.

In this work, our SOLT calibration is performed at the WR-28 reference plane after unmounting the transmit and receive antennas. WR-28 adapters, and the associated coaxial cabling, are brought physically close together to perform the SOLT calibration; as the cables are in an un-mounted state for this calibration we refer to this as the "relaxed" state, in contrast to the "mounted" state when the antenna and cables are mounted onto the robotic positioner. We use the NIST MUF to perform the VNA calibrations for our synthetic-aperture measurements [36]. This software performs VNA calibrations, as well as many other operations of interest for radio-frequency (RF) metrology, and provides an uncertainty analysis for the entire processing chain. The sources of uncertainty in a VNA measurement include the mechanical tolerances of the calibration artifacts, drift in the VNA local oscillator, and phase errors due to cable bending (see Section V-C). Fig. 10 shows the magnitude of the frequency-domain response measured by SAMURAI at a single spatial sample after it has been corrected using the SOLT calibration with the MUF. Also shown is the associated uncertainty.
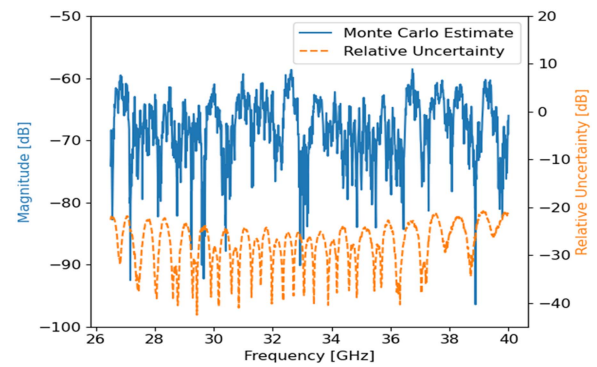

FIGURE 10. Monte Carlo estimate of the frequency response of one position in the synthetic aperture array based on an LSNA measurement and uncertainties related to its calibration. The magnitude (left axis) and its associated relative uncertainty (right axis) are shown.

C. CABLE MOVEMENT

During a synthetic-aperture measurement the probe antenna is moved through multiple spatial locations in the aperture volume. This probe is connected via a coaxial cable to the VNA and mounted to our robotic positioner. As the robot moves the probe to each position, this coaxial cable moves, flexes, and bends. These physical changes modify the electrical response of the cable in non-deterministic ways. That is, one cannot easily specify a model for the response of a cable under these states. Thus, we turn to an aleatory evaluation of the spread of the possible response of the cable. This study is presented in [37] and we summarize the methods and findings below.

After the SOLT calibration, the adapters are mounted and, in turn, each of the short-open-load standards are connected. Next the synthetic-aperture measurement for each standard is performed so that we obtain measurements of each of these standards at all of the positions. With these data, we can then use one of the following three methods to calibrate the response at each measurement point:

1) Use each unique calibration, at each measurement point, to correct the synthetic-aperture measurements at every location
2) Combine the calibrations at all points in a Monte Carlo analysis to capture the spread of the calibrations, and use this single calibration to correct the synthetic-aperture measurements at all locations
3) Use a separate calibration for positions in the synthetic aperture which are expected to have similar cable responses or states, i.e. choose a new position to use as the reference calibration when the cable experiences a large movement.

Note that for method (1) above, as our calibration procedure also includes a Monte Carlo uncertainty analysis, this method can require a lot of data (the size of the Monte Carlo sample by the number of measurements by the number of frequency points). Method (2) on the other hand allows us to reduce the size of the associated data but conflates cable response variation across positions with uncertainty at a given position.
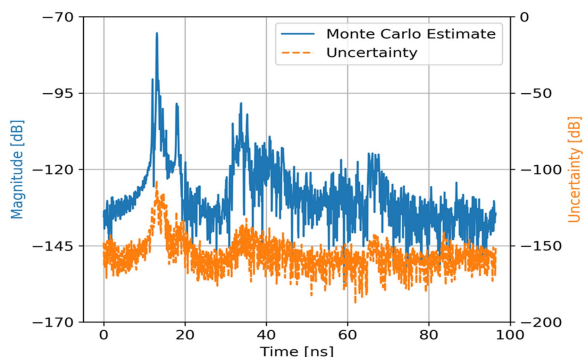
FIGURE 11. Estimated PDP and associated uncertainty when the synthetic-aperture system's calibrated frequency-domain measurements, and associated Monte Carlo samples, are transformed via beamforming and the inverse Fourier Transform.

The hybrid approach, method (3), reduces the amount of calibrations but corrects for changes in the cable response after the cable has moved significantly.

Since a random Monte Carlo iteration used to evaluate the uncertainty in a VNA/LSNA measurement at a single synthetic-aperture spatial sample includes a collection of physically-relevant errors, we can use each Monte Carlo iteration at a single spatial position along with the corresponding iterations from other positions, as well as further post-processing techniques, to generate uncertainties in communication channel metrics. Fig. 11 shows the result of beamforming the measured array samples into a specific direction by computing the frequency-domain response in that direction, and then performing the inverse Discrete Fourier Transform (IDFT) to obtain a (time-domain) power delay profile (PDP). Here we show the average of the Monte Carlo PDP realizations and the associated uncertainty at each delay sample. To keep the size of the calibration data set manageable and to control the execution time, procedure (2) described above was used to calibrate and correct the measurements that generated Fig. 11.

Note that the included uncertainties in this example are due only to uncertainties in the calibration standards, VNA drift, and cable bending. While the VNA calibration can be made traceable, the drift and cable bending calibrations are based on repeated measurements of traceable quantities. Some calculated uncertainties are shown in Figs. 10 and 11, and even though the illustrated uncertainties are quite small, they shouldn't be taken to be an accurate estimate of our entire uncertainty. Instead these plots demonstrate our ability to propagate uncertainties through the system and to obtain physically relevant values that preserve error correlations at the output of transformations such as beamforming and the IDFT. In contrast, the root-sum-squares (RSS) method does not preserve any correlations between input measurement errors when the processing output errors are reported. By ignoring correlations, an RSS-based method can greatly underestimate or overestimate uncertainty. As part of our continuing efforts, we are working to extend our uncertainty analysis to include other sources of uncertainties. We outline some of these sources in the remainder of this section.

D. RESPONSE OF THE PROBE ANTENNA

In order to accurately characterize the wireless channel, it is necessary to de-embed the probe antenna response from our over-the-air measurements. This is especially important for the current work as we typically perform measurements over a wide bandwitdh (13.5 GHz). Although analytic expressions for antenna responses exist [38] and simulations can provide an estimate of the antenna response, analytically capturing the full complexity of the antenna is non-trivial. A better approach is to measure the complex far-field antenna pattern as a function of angle, frequency and polarization [39]. Our initial step in these measurements is to estimate antenna gain using the procedures described in [40]. Second, the antenna pattern is measured on a grid of azimuth, elevation, and polarization angles. These values are normalized to the previously determined on-axis calibrated gain [39]. Throughout this process, we account for residual VNA calibration errors, positional uncertainties, and cable bending effects. We are working on incorporating these sources of uncertainty into the antenna response and may then propagate these uncertainties into the channel responses by de-embedding the antenna pattern. Note that the uncertainty in the antenna response is traceable to the meter, frequency, and impedance.

E. POSITIONING UNCERTAINTY

The locations of spatial samples in the synthetic aperture are parameters that enter the post-processing through the steering vectors used in Fourier processing, and in other algorithms. For example, the sample locations, and their errors (which can be made traceable to the meter), are used explicitly in beamforming (1) since the separation between array elements determines the inter-element phase shift required to steer the beam to a given angle. In order to accurately account for positional uncertainty we must explicitly track robot positions and use these data in our analysis.

If the antenna position errors are isotropic and uncorrelated, then the corresponding phase errors are independent random variables and would cancel out in the mainbeam of the array response [41]. However, some exploratory analysis for robotic positioners has shown that correlated position errors can create noticeable spurious lobes in the beamformed array output. One option for estimating the uncertainty in these positions is to provide a model for the robotic position [41] and estimate the positional errors through variability of parameters in the model. However, this approach requires an accurate model of the particular robot. A more effective strategy is to use an optical camera system that tracks the robot, antenna, and objects in the scene and provides accurate real-time position estimates.

Our optical system utilizes a suite of 10 cameras, each with a 51° field of view, mounted along the periphery of the measurement environment to take snapshots, at 30 or 180 frames per second, of markers placed on objects in the
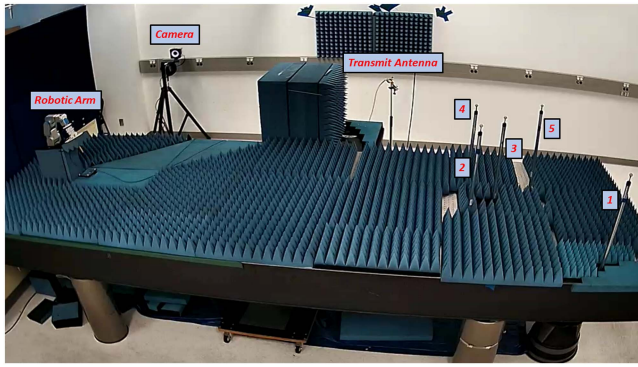
FIGURE 12. Optical table configuration of five cylinders. The LSNA is out of view behind the block of absorber near the center of table (Photograph from [23]).

scene [42]. Once calibrated, the camera system synchronizes the multiple snapshots and triangulates the locations of the markers to an accuracy on the order of 100 μm. Markers are typically placed on the receive antenna to track the six degrees-of-freedom pose of the antenna, as well as any tilt or rotation in the sampling plane of the synthetic aperture. Since the position accuracy of the optical markers is much better than the accuracy of the robot encoder that estimates the location of the robot tip, the optical markers can be used to generate accurate estimates of the measurement locations, which are in turn included in the array steering vectors, providing accurate angle estimates from a variety of algorithms. The cylinder experiment described in Section VI leverages the camera system to provide ground-truth angle and delay values and Fig. 12 shows how the cameras are placed around the optical table.

The position error estimated at each spatial sample of a planar 35-by-35 lattice is defined as the difference between the desired coordinates of the sample and the actual coordinates of the robot tip. The maximum estimated position error of the robot tip in both the x and y coordinates is 425 μm and the average error is 212.5 μm. By using the camera system these errors may be corrected. A useful goal for position error is $\lambda/50$ which corresponds to 150 μm at 40 GHz. With the 100 μm accuracy of our camera system this position error can be confirmed.

F. SCATTERING OFF POSITIONERS
Our robotic arm positioner (and any positioner) will change the RF channel through the scattering of propagating electrical signals. For a given measurement position in a synthetic aperture, the robot assumes a unique pose. This pose affects the channel as incoming signals are scattered off of the robot.[1] As our synthetic-aperture measurements contain many (typically $\approx 10^3$) individual measurement positions, each with a unique

pose, accounting for the fields scattered off the measurement equipment, including the robot, is a challenging problem.

Within our uncertainty framework we account for the measurement uncertainty attributed to extraneous fields scattering off the robot by using an aleatory method that relies on collecting multiple measurements and estimating the spread in measured S_{21} parameters when the robot's position is perturbed slightly. Since the collection of points within the spatial sampling lattice implicitly incorporates the fields scattering off the robot, we can estimate the effect of this scattering by taking multiple different synthetic-aperture measurements, each using a different set of robot poses. That is, we plan to measure a given channel using multiple, say n, synthetic-aperture measurements varying the poses in each of the $i = 1, \ldots, n$ measurements. As the ith synthetic-aperture measurement produces an estimate of the static channel (and the scattering off of the positioner changes between each measurement) we can estimate the variability of the channel due to this scattering using the spread of these measurements. This component of uncertainty is based on repeated VNA measurements, which are traceable quantities as discussed earlier.

VI. EXAMPLE: REFERENCE-SPATIAL-CHANNEL PARAMETER ESTIMATION
As mentioned in the introduction, the SAMURAI system may be used in a comparison-to-reference verification technique, providing a reference to which a DUT's output may be compared, If the DUT is a channel sounder, the sounder's ability to correctly resolve multipath delays, magnitudes, and angles of arrival is of interest. If the DUT is a real multiple-antenna wireless device, its ability to receive, demodulate, and decode communication signals in mmWave RF channels with known timing and spatial characteristics is tested. Either way, an essential part of such a comparison is the parameter estimation algorithm used to extract the key channel features such as angle of arrival. We present two approaches for extracting the angle of arrival of multipath components, providing an illustration of the resolution capabilities of the SAMURAI system. First, we describe a measurement experiment using five aluminum cylinders configured on an optical table as shown in Fig. 12 such that they create a wireless reference channel.

A. FIVE-CYLINDER EXPERIMENT
This experiment using 5 aluminum cylinders was conducted to test the resolution capabilities of SAMURAI. A 6-inch OEWG antenna was used on receive. Fig. 13 illustrates the ground-truth locations of five cylinders measured on the surface of an optical table using the ancillary camera system and Fig. 12 is a picture of the experiment configuration. Since the cylinders were vertically oriented and resting directly on the optical table in the same plane as the coordinate system origin, their y-coordinates are constant values. Note that cylinders two and three were placed within the same beamwidth and cylinders four and five were placed to create nearly equal
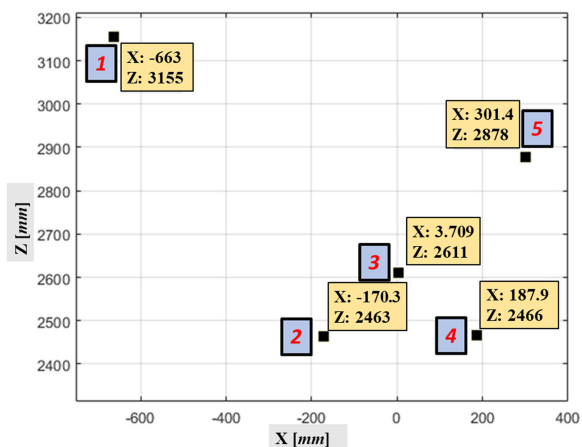
---

[1]Note that while placing RF absorber on the positioner may reduce scattering, the positioner will still have a non-negligible impact on the channel, especially at mmWave frequencies where RF absorber is less ideal.

FIGURE 13. Top-down view of the optical table showing the location of the five aluminum cylinders used to verify the resolution capabilities of SAMURAI.

FIGURE 14. Orthogonal projections: iteration one. Cylinders three and four are visible.

FIGURE 15. Orthogonal projections: iteration two. Projecting the data into a direction orthogonal to cylinder three improves the AoA estimate for cylinder four.

signal path lengths between the transmit and receive antennas. This configuration was intended to test the ability of lower-resolution channel sounders to discern the temporal and spatial features of the propagation environment. The receive antenna was located at the origin of the plot in Fig. 13 and the transmit antenna is radiating from a direction towards the lower-right corner.

B. NARROWBAND ANGLE ESTIMATION

Angle estimation algorithms such as MUSIC, SAGE, ES-PIRIT, Maximum Likelihood, and others rely on steering vectors to describe the array manifold (defined as the locus of all array response vectors) [18]. Steering vectors implicitly assume the received signal is narrowband since each component of the vector is a phase shift that corresponds to the propagation time between array elements. The narrowband assumption is valid for SAMURAI since the VNA/LSNA uses continuous-wave (CW) tones to measure S-parameters. Measuring phase precisely and accurately at a single frequency enables the accurate estimation of the angles of arrival (AoAs) for multipath in wireless channels. If a simultaneous estimate of delay is not necessary, then angle estimation is best performed at the highest available frequency. Here we use 40 GHz because the array beamwidth is the most narrow and provides the greatest angular resolution.

The signal model defined in Appendix A describes the array element signals measured at each frequency as a superposition (summation) of impinging plane waves with infinitesimal bandwidth arriving from point sources. Using this model it is possible to estimate multipath angles of arrival using a nested sequence of orthogonal projections. Each projection removes an individual plane wave incident on the aperture from the measured signal until the norm of the array output vector is minimized.

Algorithm 1 in Appendix A implements this approach for angle estimation by iteratively projecting the measured array output vector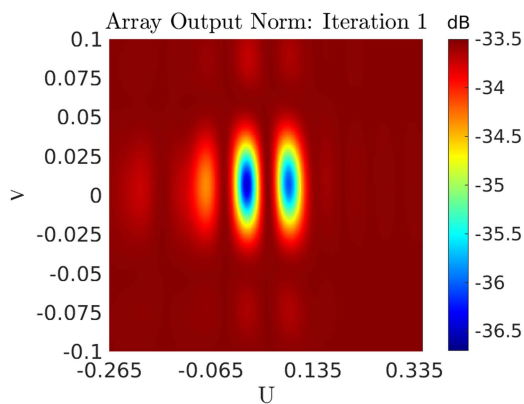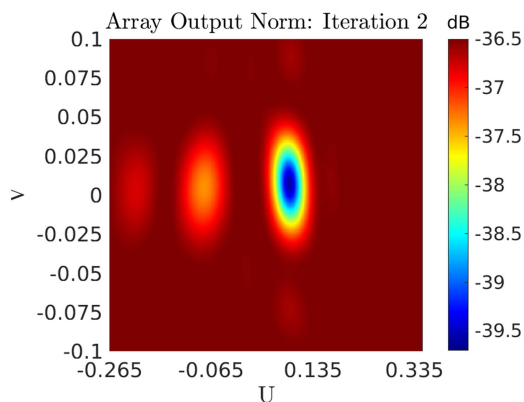 onto the subspace orthogonal to a chosen search direction. If the search direction is orthogonal to one of the plane waves contained in the received signal, then the norm of the projected array output vector will decrease and be less than the norm of the array output vector before the projection operator was applied. By finding the direction at each algorithm iteration that yields the minimum norm for the projected array output vector, the angle of arrival for each scatterer in the scene can be estimated. After each angle is estimated, the corresponding steering vector is accumulated along with the previous steering vectors before computing the next projection operator. In this manner, any leakage of the projected array output vector into previously visited subspaces is minimized.

The ground-truth path length computed for a particular cylinder is equal to the sum of the Euclidean distance in the xz plane from the transmit antenna to the cylinder and from the cylinder to the receive antenna at the origin. Figs. 14 and 15 illustrate the cost function for the first two iterations of Algorithm 1 using the five-cylinder data set. Cylinders three and four are clearly visible in the first iteration after which a null is placed in the estimated direction of cylinder four. Fig. 16 plots the maximum and minimum values in dB for the cost function which clearly illustrate that the algorithm is
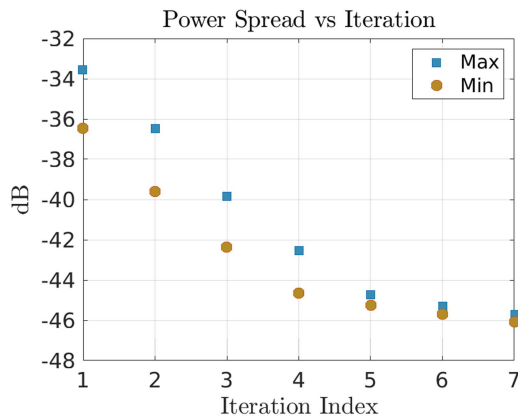
FIGURE 16. Narrowband algorithm convergence illustrating the maximum and minimum values, in dB, of the cost function. The decreasing spread between maximum and minimum values of the cost function clearly illustrates that the orthogonal-projections algorithm is converging.

TABLE 2 Angle Estimation Performance: Five Cylinders

Nbr.	Truth True Az True El (deg)	NB Estimate Est Az Est El (deg)	NB Estimate Error Az Error El (deg)	WB Estimate Est Az Est El (deg)	WB Estimate Error Az Error El (deg)
1	-11.87 0	-12.71 0.18	0.84 -0.18	-12.75 0.88	0.88 -0.88
2	-3.96 0	-4.86 0.25	0.91 -0.25	-4.62 0.38	0.67 -0.38
3	0.08 0	0.3 0.36	-0.22 -0.36	0.38 0.13	-0.29 -0.13
4	4.36 0	5.13 0.40	-0.78 -0.40	4.88 0.13	-0.52 -0.13
5	5.98 0	8.07 -0.07	-2.09 0.07	6.75 0.63	-0.77 -0.63

converging. Table 2 lists the estimated angles of arrival for each cylinder and the error compared to ground-truth values measured using the optical camera system. The narrowband angle estimation results show excellent angle estimation performance with a maximum error of 2.1° for cylinder five. Wideband angle estimation performance will be described in the next section. Both the narrowband and wideband angle estimation results presented are based on measurements that have been corrected via the NIST MUF to account for calibration errors in the VNA. [36]

C. WIDEBAND PROCESSING

In dense multipath environments, wideband synthetic apertures that sample over a large spatial area are desirable because they can provide the delay and angle resolution necessary to detect the fine features of received multipath. Care must be taken however in the back-end Fourier processing to account for the wide bandwidth of the system. For example, one consequence of wide signal bandwidths is that beam

squint will have an appreciable effect on angle estimation performance [43]. Beam squint refers to the change in pointing direction of the array main beam when phase shift steering is applied over wide signal bandwidths. The first stage in wideband processing is the use of true time delay beam steering to eliminate beam squint. The second stage is the computation of PDPs for specified directions and the third stage is the formation of "delay slices" at specified delay values. These processing steps are described next.

1) TRUE TIME DELAY BEAM STEERING TO GENERATE POWER ANGLE DELAY PROFILES

Steering the array response in narrowband regimes consists of inserting a single phase shift behind each array element that compensates for the incremental propagation delay between the elements. For wideband systems however, a pure time delay (or equivalently a phase shift that varies linearly with frequency) must be inserted behind each array element to steer the beam and to avoid beam squint [44]. Since synthetic aperture systems like SAMURAI digitize the received signal at every spatial sample, it is possible to apply in software a linear versus frequency steering-phase term, ψ, at the mnth array element according to [44],

$$\psi_{mn}(\theta, \phi) = \frac{2\pi f}{c}(x_m \sin\theta \cos\phi + y_n \sin\theta \sin\phi). \quad (5)$$

To steer the beam, the frequency-dependent phase $\psi_{mn}(\theta, \phi)$ is applied to the S_{21} parameters measured at the mnth spatial sample. After transforming the result to the time domain via an IDFT, the result is the signal voltage received versus delay from the direction (θ, ϕ). Taking the magnitude squared of this time series yields the power angle delay profile (PADP) with peaks that correspond to sources of scattered signal energy. An optional step to increase the sampling resolution of the PADP is to zero-pad the frequency domain beam output before computing the IDFT. Since the zero padding operation will induce significant ripple in the delay domain due to the wideband nature of the data, a window function, such as Hamming, should be applied to the frequency domain samples. Algorithm 2 in Appendix B lists the precise steps for computing the output of wideband beamforming.

2) DELAY SLICES

If a PADP is computed for every direction in space, the result is a four-dimensional view of the channel impulse response (CIR) that provides power received versus delay, azimuth, and elevation. A "delay slice" through the CIR consists of power received versus all angles for a fixed delay bin. Delay slices are especially useful for pinpointing the spatial direction of strong multipath that arrives at a single delay bin. Algorithm 2 lists the steps for computing delay slices. First, directional PADPs are computed for a discrete grid of K beam-steering angles, (θ_k, ϕ_k) or (u_k, v_k), that cover the entire forward hemisphere, or a smaller sector. Next, the power at the fixed delay $\tau = \tau_m$ is extracted from each PADP. The result is $x(\tau_m; u, v)$ which represents the spatial frequency spectrum at τ_m with

peaks corresponding to the angles of arrival for multipath sources.

The delay slices can be computed slightly faster by evaluating the IDFT at a single delay $\tau = \tau_m$ directly instead of computing the IDFT for all delays. The IDFT of the frequency domain beam output $b(f_s; u_k, v_k)$ computed for the mth delay bin τ_m is

$$x(\tau_m; u_k, v_k) = \frac{1}{S} \sum_{s=0}^{S-1} b(f_s; u_k, v_k) e^{j2\pi ms/S} \qquad (6)$$

where S is the total number of frequency samples and also $0 \le m \le S - 1$.

Delay slices computed using Algorithm 2 are very effective for pinpointing multipath sources when a set of delay bins is determined apriori for search. A powerful technique for quickly identifying the strongest multipath sources is to compute the total received power versus delay over all spatial directions. This straightforward computation requires integrating (using summation) the power received over all angles for each delay slice $x(\tau_m; u, v)$ as in,

$$r(\tau_m) = \sum_{k=0}^{K-1} |x(\tau_m; u_k, v_k)|^2. \qquad (7)$$

The result is a new power delay profile $r(\tau_m)$ that represents total power received by the synthetic aperture versus delay. Local peaks in $r(\tau_m)$ identify the time instants where CIR delay slices would be of interest.

D. JOINT DELAY-ANGLE ESTIMATION

As described previously, five aluminum cylinders were arranged in a deliberate configuration to test the resolution limits of SAMURAI. Cylinders four and five were placed in the same beamwidth and cylinders two and three were situated in the same delay bin. Algorithm 2 and (7) were used to compute total energy received versus delay and to identify the delay bins with strong reflections that might contain the cylinders. For these computations, a Hamming window was applied to the frequency output of each beam and the result was zero padded to a total length four times longer than the original. Figs. 17 and 18 illustrate the output of this processing. Fig. 19 shows the estimated spatial frequency spectra at the delay bins corresponding to the cylinders. Cylinder three is clearly visible near the boresight direction, cylinders two and three appear in the same delay bin but at different angles, and cylinders four and five appear in the same beam but at different delay bins. Cylinder one is isolated in delay and angle compared to the other cylinders.

The wideband multipath extraction method described in this section has successfully resolved cylinders four and five in delay and cylinders two and three in angle. Note that zero padding improves the multipath estimation performance because the spatial frequency spectrum may vary significantly between delay bins. Table 2 lists the estimated angles of arrival for each of the five cylinders along with the errors computed with respect to the measured cylinder locations on
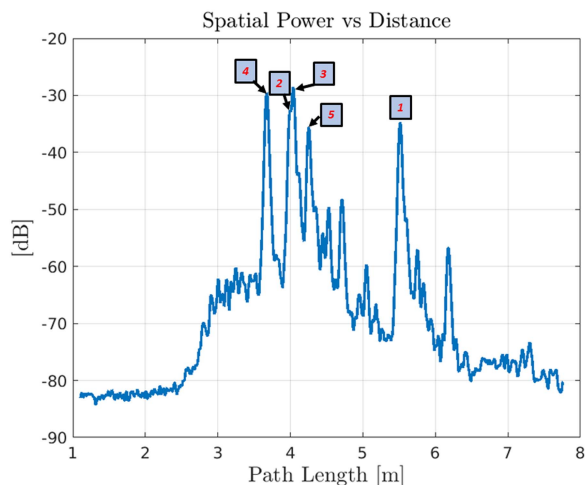

FIGURE 17. Total received power normalized by the transmit power as a function of distance from the Rx array computed over a ±20° sector for the five-cylinder scattering experiment.

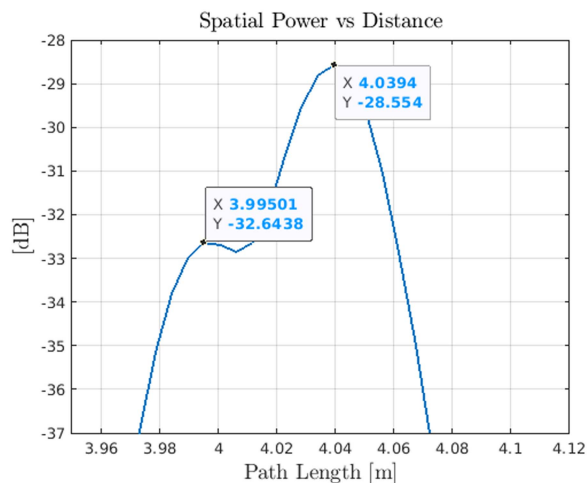**FIGURE 18. Close-up of cylinder two (left marker) and cylinder three (right marker).**

TABLE 3 Delay Estimation Performance: Five Cylinders

Nbr.	True Path Length (m)	Estimate (m)	Error (m)
1	5.54	5.54	-0.004
2	4.02	4.02	0.0036
3	4.07	4.07	0.0094
4	3.69	3.70	-0.0025
5	4.27	4.27	-0.0110

the optical table. Table 3 lists the estimated and true path lengths corresponding to each cylinder.

VII. CONCLUSION

Wideband synthetic-aperture systems that utilize LSNAs or VNAs, along with the associated post-processing algorithms described in this paper, are capable of making accurate, high-resolution estimates of the delays, angles of arrival, and path
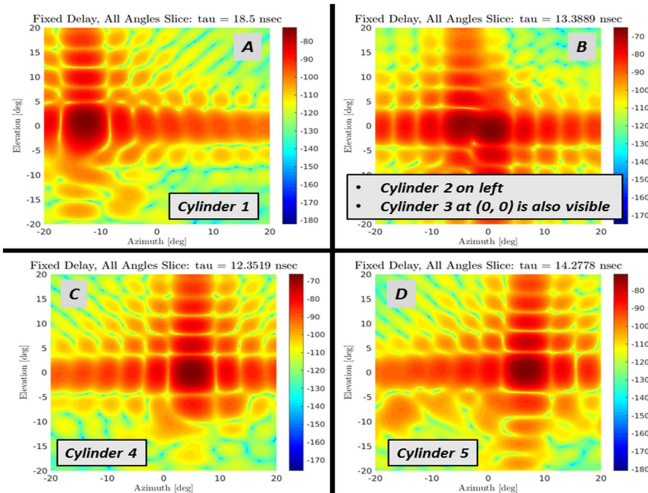
FIGURE 19. A) The channel impulse response at a specific time delay (or "delay slice") as a function of elevation and azimuth. **B)** Close-up of cylinder two (left peak) and cylinder three (right peak). Both cylinders appear in same delay bin. **C)** Cylinder 4. Note cylinders 4 and 5 appear in the same beam but different delay bins, 12.35 and 14.27 nsec respectively. **D)** Cylinder 5.

loss associated with multipath in static wireless communication channels. By characterizing the wireless-propagation environment to a high degree of fidelity, measurements from such systems may be used as a reference to which other, lower resolution instrumentation may be compared.

LSNA-based synthetic aperture systems have the additional advantage of providing wave parameters that are calibrated in magnitude and relative phase, which is useful for evaluating wireless DUTs involving modulated signals and those involving frequency conversion. When combined with a traceable uncertainty analysis that incorporates the impact of errors and uncertainties into the final channel-parameter estimates of wireless-communication metrics, such a system can be used in OTA calibrations.

We presented a systematic method for determining system parameters such as aperture size, dynamic range, measurement bandwidth, and unambiguous signal duration. In addition, we provided highly accurate narrowband or wideband angle and delay estimation algorithms.

Furthermore, our framework for uncertainty analysis maintains the correlations between components of uncertainty as they are propagated (traceably) from fundamental standards to derived quantities. Sources of measurement uncertainty considered in this framework include calibration errors in the LSNA or VNA, uncertainties in the complex pattern of the receive antenna, position errors as the robot traverses through the spatial sampling lattice, and errors in the camera or sensor system used to determine ground-truth values for scatterers.

Additional research being conducted by NIST focuses on the three key aspects of the SAMURAI system discussed here: the precision hardware, the correlated, traceable uncertainty analysis, and the parameter estimation algorithms.

Such research will extend the uncertainty analysis and traceability associated with synthetic-aperture measurements to further validate the utility of synthetic apertures as reference instruments, over-the-air calibration standards, and spatial metrology tools. The rigorous tools for wireless metrology developed at millimeter wave frequencies with SAMURAI may also be extended to the THz regime in future work.

APPENDIX A
NARROWBAND ANGLE ESTIMATION ALGORITHM

Algorithm 1: Angle Estimation Using Orthogonal Subspace Projections.

INPUTS:
1: At the jth iteration, the previous projected array output vector $\mathbf{y}_{j-1}$. The vector $\mathbf{y}_0$ is equal to the measured array output vector at 40 GHz.
2: At the jth iteration accumulate the unit norm steering vectors corresponding to previously estimated angles of arrival into the columns of the matrix $\mathbf{T} = [\mathbf{a}(u_0, v_0) \dots \mathbf{a}(u_{j-1}, v_{j-1})]$.

COMPUTATIONAL STEPS:
1: $\mathbf{R} \leftarrow \mathbf{T}\left(\mathbf{T}^H\mathbf{T}\right)^{-1}\mathbf{T}^H$
2: $\mathbf{P}_j \leftarrow \mathbf{I} - \mathbf{R}$
3: $\mathbf{y}_j \leftarrow \mathbf{P}_j\mathbf{y}_{j-1}$
4: Construct a dense uniformly sampled grid of L angles; $\{(u_l, v_l)|l = 0, \dots, L-1\}$
5: Compute the unit norm steering vector $\mathbf{a}(u_l, v_l)$
6: $\widetilde{\mathbf{P}}_l \leftarrow \mathbf{I} - \mathbf{a}(u_l, v_l)\mathbf{a}(u_l, v_l)^H$
7: $\widetilde{\mathbf{y}}_l \leftarrow \widetilde{\mathbf{P}}_l\mathbf{y}_j$
8: $n_l \leftarrow \widetilde{\mathbf{y}}_l^H\widetilde{\mathbf{y}}_l$
9: Find the direction (u_{min}, v_{min}) that minimizes n_l over all l. This direction becomes the estimated angle of arrival for the jth multipath component
10: Proceed to the $(j+1)$st algorithm iteration

The signal measured at each element of an array can be modeled as a sum of K impinging plane waves. The contribution of the kth plane wave to the baseband signals in the array output vector can be written as

$$\mathbf{s}(t; u_k, v_k) = \mathbf{v}(u_k, v_k)\alpha_k e^{j2\pi v_k t}u(t - \tau_k) \qquad (8)$$

where $\alpha_k, \tau_k, (u_k, v_k), v_k$ are the complex amplitude, the relative delay, the angle of arrival, and the Doppler frequency of the kth wave. Note that Doppler is not estimated using a synthetic aperture since the wireless channel must be static during the duration of the robot's motion along the spatial sampling lattice to avoid coupling the spatial phase at each array element with a phase shift due to Doppler frequency. Therefore, the expression in (8) is equivalent to the S_{21} parameters measured by SAMURAI for the case where $v_k = 0$. Recall that in spherical coordinates the mth component of the $M \times 1$ steering vector corresponding to the nth source can be written as

$$[\mathbf{v}(\theta_n, \phi_n)]_m$$

$$= g_m(\theta_n, \phi_n)e^{jk(x_m \sin\theta_n \cos\phi_n + y_m \sin\theta_n \sin\phi_n + z_m \cos\theta_n)} \quad (9)$$

where $k = \frac{2\pi}{\lambda}$, (x_m, y_m, z_m) is the location of the mth array element and $g_m(\theta_n, \phi_n)$ is the voltage gain of the mth array element in the direction (θ_n, ϕ_n). In sine space coordinates, and ignoring a constant z_m term,

$$[\mathbf{v}(u_n, v_n)]_m = g_m(u_n, v_n)e^{jk(x_m u_n + y_m v_n)}. \quad (10)$$

The signal vector at the output of the array is

$$\mathbf{y}(t) = \sum_{k=0}^{K-1} \mathbf{s}(t; u_k, v_k) + \sigma \mathbf{n}(t) \quad (11)$$

where $\mathbf{n}(t)$ denotes a $M \times 1$ vector valued complex white Gaussian noise process with power σ^2. Algorithm 1 estimates the AoA for each impinging plane wave and reduces the norm of the array output vector $\mathbf{y}$ after each iteration.

APPENDIX B
WIDEBAND JOINT ANGLE-DELAY ESTIMATION ALGORITHM

Algorithm 2: Directional PDP Computation.

INPUTS:

1: Measured array output vector $\mathbf{y}(\omega_s)$ at each frequency ω_s for $s = 0, \ldots, S-1$ and a desired beam pointing direction (θ_0, ϕ_0) or (u_0, v_0)

2: The desired beam pointing direction can be determined by locating peaks in the spatial Fourier Transform output computed at 40 GHz using (2)

COMPUTATIONAL STEPS:

1: Compute the phase steering vector for each frequency, $\mathbf{w}(\omega_s; u_0, v_0)$ as in (5)

2: Beamform the array output vector $\mathbf{y}(\omega_s)$ at each frequency by forming the dot product $b(\omega_s; u_0, v_0) = \mathbf{w}(\omega_s; u_0, v_0)^H \mathbf{y}(\omega_s)$

3: Compute the length S temporal IDFT to obtain the beam output (directional PDP), $x(\tau_s; u_0, v_0) = \text{IDFT}[b(\omega_s; u_0, v_0)]$

4: **To increase sampling resolution** : compute a window function $w(s)$ of length S with low sidelobes, e.g. Hamming window. Zero-pad the sequence $w(s)b(\omega_s; u_0, v_0)$ to L times its original length and compute the IDFT

5: For the fixed delay $\tau = \tau_0$, $x(\tau_0; u, v)$ is the spatial frequency spectrum of all signal sources impinging on the array (also called a delay slice) and can be used to estimate angles of arrival

---

REFERENCES

[1] J. A. Jargon, J. T. Quimby, K. A. Remley, A. A. Koepke, and D. F. Williams, "Verifying the performance of a correlation-based channel sounder in the 3.5 GHz band with a calibrated vector network analyzer," in *Proc. IEEE Asia-Pacific Microw. Conf.*, 2019, pp. 387–389.

[2] H. Hayashi and T. Ohtsuki, "DOA estimation in MIMO radar using temporal spatial virtual array with MUSIC algorithm," in *Proc. 9th Int. Conf. Signal Process. Commun. Syst.*, 2015, pp. 1–6.

[3] A. Mannesson, B. Bernhardsson, M. A. Yaqoob, and F. Tufvesson, "Optimal virtual array length under position imperfections," in *Proc. IEEE 8th Sensor Array Multichannel Signal Process. Workshop*, 2014, pp. 5–8.

[4] G. Santella and E. Restuccia, "Analysis of frequency domain wide-band measurements of the indoor radio channel at 1, 5.5, 10 and 18 GHz," in *Proc. IEEE Glob. Commun. Conf.*, 1996, pp. 1162–1166.

[5] S. J. Howard and K. Pahlavan, "Measurement and analysis of the indoor radio channel in the frequency domain," *IEEE Trans. Instrum. Meas.*, vol. 39, no. 5, pp. 751–755, Oct. 1990.

[6] M. H. C. Dias and G. L. Siqueira, "Indoor 1.8 GHz AOA-TDOA measurements extending the use of a wideband propagation channel sounder with the synthetic aperture concept," in *Proc. Eur. Microw. Conf.*, 2005, pp. 4–1194.

[7] A. W. Mbugua, W. Fan, Y. Ji, and G. F. Pedersen, "Millimeter wave multi-user performance evaluation based on measured channels with virtual antenna array channel sounder," *IEEE Access*, vol. 6, pp. 12318–12326, 2018.

[8] S. Ranvier, M. Kyro, K. Haneda, T. Mustonen, C. Icheln, and P. Vainikainen, "VNA-Based wideband 60 GHz MIMO channel sounder with 3-D arrays," in *Proc. IEEE Radio Wireless Symp.*, 2009, pp. 308–311.

[9] H. Qiao, P. Sarangi, Y. Alnumay, and P. Pal, "Sample complexity trade-offs for synthetic aperture based high resolution estimation and detection," in *Proc. IEEE 11th Sensor Array Multichannel Signal Process. Workshop*, 2020, pp. 1–5.

[10] B. Chen, Z. Zhong, B. Ai, and D. G. Michelson, "Moving virtual array measurement scheme in high-speed railway," *IEEE Antennas Wireless Propag. Lett.*, vol. 15, pp. 706–709, 2016.

[11] T. Zhou, C. Tao, S. Salous, and L. Liu, "Measurements and analysis of angular characteristics and spatial correlation for high-speed railway channels," *IEEE Trans. Intell. Transp. Syst.*, vol. 19, no. 2, pp. 357–367, Feb. 2018.

[12] H. Nguyen, K. Mahler, M. Peter, W. Keusgen, T. Eichler, and H. Mellein, "Estimation of DoA based on large scale virtual array data," in *Proc. 10th Eur. Conf. Antennas Propag.*, 2016, pp. 1–4.

[13] M. Kyro, S. Ranvier, V. M. Kolmonen, K. Haneda, and P. Vainikainen, "Long range wideband channel measurements at 81-86GHz frequency range," in *Proc. 4th Eur. Conf. Antennas Propag.*, 2020, pp. 1–5.

[14] H. Nguyen, W. Keusgen, and T. Eichler, "Instantaneous direction of arrival measurements in mobile radio channels using virtual circular array antennas," in *Proc. IEEE Glob. Commun. Workshops*, 2016, pp. 1–7.

[15] M. G. Becker, R. D. Horansky, D. Senic, V. Neylon, and K. A. Remley, "Spatial channels for wireless over-the-air measurements in reverberation chambers," in *Proc. 12th Eur. Conf. Antennas Propag.*, 2018, pp. 1–5.

[16] A. J. Weiss et al., "Large-signal network analysis for over-the-air test of up-converting and down-converting phased arrays," in *Proc. IEEE MTT-S Int. Microw. Symp. Dig.*, 2019, pp. 622–625.

[17] Joint Committee for Guides in Metrology, "Evaluation of measurement data–guide to the expression of uncertainty in measurement," 2008. [Online]. Available : https://www.bipm.org/en/publications/guides

[18] R. L. Haupt, *Antenna Arrays: A Computational Approach*. Hoboken, NJ, USA: Wiley, 2010.

[19] J. Fordham et al., "IEEE Recommended Practice for Antenna Measurements," *Antennas Propag. Standards Committee IEEE Antennas Propag. Soc.*, vol. 64, no. 3, pp. 143–143, Jun. 2022.

[20] G. F. Masters and S. F. Gregson, "Coordinate system plotting for antenna measurements," *NSI-MI Inc.* Suwanee, GA, USA, Tech. Rep. 92, 2007.

[21] R. J. Mailloux, *Phased Array Antenna Handbook*. Norwood, MA, USA: Artech House, 2005.

[22] P. Vouras et al., *Metrology for 5G and Emerging Wireless Technologies*, T. H. Loh, Ed. London, U.K.: IET, 2021.

[23] D. Guven et al., "Methodology for measuring the frequency dependence of multipath channels across the millimeter-wave spectrum," *IEEE Open J. Antennas Propag.*, vol. 3, pp. 461–474, 2022.

[24] B. Porat, *A Course in Digital Signal Processing*. Hoboken, NJ, USA:Wiley, 1997.

[25] "Keysight 2-port and 4-port PNA-X network analyzer: Data sheet and technical specifications for N5244A and N5245A analyzers," *Keysight Technol.*, 2018.

[26] J. Hejselbaek, W. Fan, and G. F. Pedersen, "Ultrawideband VNA based channel sounding system for centimetre and millimetre wave bands," in *Proc. 27th IEEE Annu. Int. Symp. Personal, Indoor, Mobile Radio Commun.*, 2016, pp. 1–6.

[27] A. M. Street, L. Lukama, and D. J. Edwards, "Use of VNAs for wide-band propagation measurements," *IEE Proc. Commun.*, vol. 148, no. 6, pp. 411–415, 2001.

[28] C. U. Bas, V. Kristem, R. Wang, and A. F. Molisch, "Real-time ultra-wideband channel sounder design for 3–18 GHz," *IEEE Trans. Commun.*, vol. 67, no. 4, pp. 2995–3008, Apr. 2019.

[29] J. N. H. Dortmans, J. T. Quimby, K. A. Remley, D. F. Williams, J. Senic, and R. Sun, "Design of a portable verification artifact for millimeter-wave-frequency channel sounders," *IEEE Trans. Antennas Propag.*, vol. 67, no. 9, pp. 6149–6158, Sep. 2019.

[30] A. J. Weiss et al., "Setup and control of a millimeter-wave synthetic aperture measurement system with uncertainties," in *Proc. 95th Autom. Radio Freq. Techn. Group Microw. Meas. Conf.*, 2020, pp. 1–4.

[31] "Meca500 (r3) user manual: Robot firmware 7.0.6, document revision F," *Mecademic Inc*, Nov. 12, 2018.

[32] A. J. Weiss, "SAMURAI documentation," 2020. [Online]. Available: www.nist.gov/services-resources/software

[33] Joint Committee for Guides in Metrology, "International vocabulary of metrology–basic and general concepts and associated terms," 3rd ed., 2008. [Online]. Available: https://www.bipm.org/en/publications/guides

[34] K. A. Remley, D. F. Williams, P. D. Hale, C. Wang, J. Jargon, and Y. Park, "Millimeter-wave modulated-signal and error-vector-magnitude measurement with uncertainty," *IEEE Trans. Microw. Theory Techn.*, vol. 63, no. 5, pp. 1710–1720, May 2015.

[35] J. A. Jargon, D. F. Williams, and P. D. Hale, "Developing models for type-n coaxial VNA calibration kits within the NIST microwave uncertainty framework," in *Proc. 87th Autom. Radio Freq. Techn. Group Microw. Meas. Conf.*, 2016, pp. 1–4.

[36] D. F. Williams, "NIST microwave uncertainty framework," 2019. [Online]. Available: www.nist.gov/services-resources/software/wafer-calibration-software

[37] A. J. Weiss, "Characterization of a vector network analyzer based millimeter-wave channel sounder," Master's Thesis, Colorado School of Mines, Golden, CO, USA, 2018.

[38] C. A. Balanis, *Antenna Theory: Analysis and Design*. Hoboken, NJ, USA: Wiley, 2005.

[39] A. J. van den Biggelaar, B. F. Jamroz, D. F. Williams, A. B. Smolders, and U. Johannsen, "Correction of the measured phase of the radiation pattern of millimeter-wave antennas," in *Proc. Antenna Meas. Techn. Assoc. Conf.*, 2020, pp. 1–5.

[40] A. Newell, R. Baird, and P. Wacker, "Accurate measurement of antenna gain and polarization at reduced distances by an extrapolation technique," *IEEE Trans. Antennas Propag.*, vol. 21, no. 4, pp. 418–431, Jul. 1973.

[41] J. Denavit and R. S. Hartenberg, "A kinematic notation for lower-pair mechanisms based on matrices," *Trans, ASME E. J. Appl. Mechanics*, vol. 22, pp. 215–221, 1955.

[42] R. Bostelman, J. Falco, M. Shah, and T. H. Hong, "Dynamic metrology performance measurement of a six degrees-of-freedom tracking system used in smart manufacturing," in *Autonomous Industrial Vehicles From the Laboratory to the Factory Floor*. West Conshohocken, PA, USA: ASTM International, 2016, pp. 91–105.

[43] B. Wang, M. Jian, F. Gao, G. Y. Li, and H. Lin, "Beam squint and channel estimation for wideband mmwave massive MIMO-OFDM systems," *IEEE Trans. Signal Process.*, vol. 67, no. 23, pp. 5893–5908, Dec. 2019.

[44] I. Frigyes and A. J. Seeds, "Optically generated true-time delay in phased-array antennas," *IEEE Trans. Microw. Theory Techn.*, vol. 43, no. 9, pp. 2378–2386, Sep. 1995.